J. Fluid Mech. (2025), *vol.* 1010, A32, doi:10.1017/jfm.2025.108

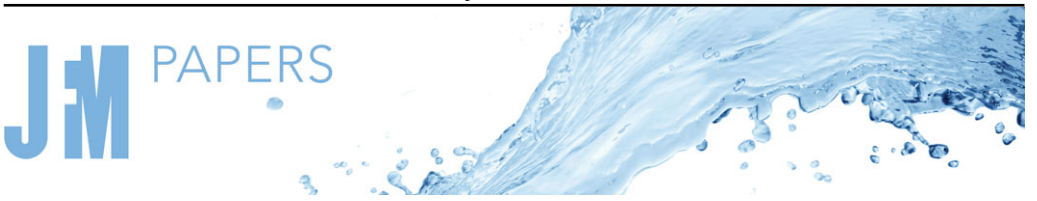

Double crown during drop impact on an immiscible shallow pool

Abdulrahman B. Aljedaani[1,2], **Muhammad F. Afzaal**[1], **Kenneth R. Langley**[1], **Zi Qiang Yang**[1] **and S.T. Thoroddsen**[1]

[1]Division of Physical Sciences and Engineering, King Abdullah University of Science and Technology (KAUST), Thuwal 23955-6900, Saudi Arabia

[2]KAUST Upstream Research Center (KURC), EXPEC Advanced Research Center, Saudi Aramco, Thuwal 23955-6900, Saudi Arabia

Corresponding author: S.T. Thoroddsen, sigurdur.thoroddsen@kaust.edu.sa

(Received 1 October 2024; revised 12 January 2025; accepted 14 January 2025)

The Edgerton crown is an iconic manifestation of drop impact splashing, with its prominent cylindrical edge decorated with detaching droplets. Herein, we identify the formation of an intriguing double-crown, when a high-viscosity drop impacts on a shallow pool of a lower-viscosity immiscible liquid. High-speed imaging shows that after the initial fine horizontal ejecta sheet, the first inner crown emerges vertically from the film liquid. This is followed by the second crown which forms near the outer base of the first crown, as the tip of the horizontally spreading viscous drop approaches the outer free surface. Axisymmetric numerical simulations, using the volume-of-fluid method with adaptive grid refinement, show that the flow squeezed out between the viscous drop and the solid surface, generates two counter-rotating vortex rings, which travel radially outwards together and drive out the second crown through the free surface. The bottom vortex emerges from the separated boundary layer at the solid wall, while the top one detaches from the underside of the viscous drop. We map out the narrow parameter regime, where this ephemeral structure emerges, in terms of viscosity ratio, impact velocity and film thickness.

Key words: breakup/coalescence

1. Introduction

When drops impact onto liquid surfaces, the well-known Edgerton crown is often formed (Edgerton & Killian 1939) and its aesthetic shape has become the prototypical

manifestation of splashing. In addition to the beautiful pictures, splashing is important in many industrial applications and in natural phenomena, including inkjet printing (Lohse 2022), spray painting, cooling and cleaning; atomisation in combustion as well as aerosol formation and soil erosion by rain. Rein (1993) gave an early review of this phenomenon, with more recent theoretical and experimental overviews given by Yarin (2006) and Roisman, Horvat & Tropea (2006), as well as Liang & Mudawar (2016) for impacts onto liquid films.

The bowl-like crown was initially thought to rise vertically out of the liquid pool or film (Yarin & Weiss 1995), while advances in high-speed video imaging enabled the characterisation of finer details, revealing numerous previously unobserved fluid phenomena (Thoroddsen, Etoh & Takehara 2008). Principal among these is the ejecta sheet which emerges from the early neck connecting the drop and pool liquids, which precedes the crown (Weiss & Yarin 1999; Thoroddsen 2002). It has furthermore become clear that pure Edgerton crowns only arise for specific conditions at low impact velocities (Deegan, Brunet & Eggers 2007; Villermaux 2020).

One of the most representative (and consequential) stages of drop impact splashing is the ejection of secondary droplets. Understanding under what conditions and in what numbers they are produced is of practical interest. In particular, which mechanism produces the smallest droplets, which, for example, determines the number of microscopic aerosols that remain when air-born satellite droplets evaporate. These aerosols can have an impact on human health and act as nucleation sites during cloud formation (Blanchard & Woodcock 1957). Large secondary droplets, however, displace the largest amount of liquid and can lead to secondary impacts and more gas transport across the air–water interface.

Most previous drop-impact studies have examined the impact of drops onto films or pools of the same liquid – this of course being the most common configuration arising both in nature and industrial applications. Rain drops impact lakes and the Sea, and a sequence of drops impacting a solid surface quickly wets it and forms a film of the same. However, drops with different properties than the film can arise in important special cases, such as rain impacting oil slicks (Murphy *et al.* 2015; Kim *et al.* 2021; Zhang, Wang & Rui 2022) or when the temperature changes the film viscosity during spray cooling, to name only two. Fudge, Cimpeanu & Castrejón-Pita (2024) used both experiments and simulations to study how the thickness and properties of the floating oil film affects the penetration velocity, showing the great importance of high film viscosity. Earlier studies have looked at the shape evolution and breakup of miscible drops impacting deep pools of different liquids, for example, when the drop is of higher viscosity (Walker, Logia & Fuller 2015; Li, Bailharz & Thoroddsen 2017; Minami & Hasegawa 2022), showing a wide variety of shapes, including the buckling of viscous sheets.

Only a few authors have investigated the splashing from such impacts with a substrate wetted by another liquid, either experimentally (Chen, Chen & Amirfazli 2017; Geppert *et al.* 2017) or numerically (Agbaglah 2021; Fudge *et al.* 2023). When the drop and pool are of different miscible liquids, the breakup of the crown can occur through Marangoni-driven holes, as shown by Thoroddsen, Etoh & Takehara (2006) and Aljedaani *et al.* (2018). This type of breakdown is of practical significance in a number of applications, like defoaming and emulsification (Geppert *et al.* 2016).

Kittel, Roisman & Tropea (2018) analysed the splashing threshold by considering the viscosity ratio between the drop and film, and found that the properties of the lower viscosity fluid controlled the splashing dynamics. Marcotte *et al.* (2019) investigated the impact of an ethanol drop onto a pool of water–glycerin solutions both experimentally and numerically, by setting zero interfacial tension and varying the pool viscosity. They mainly identify the interface shapes and qualitative changes in orientation of the sheet

Figure 1. Example of the double crown, for a glycerine drop of diameter $D = 4.47$ mm, impacting at $U = 7.75$ m s^{-1} onto a 0.8 mm thin layer of silicone oil of viscosity 2 cSt. This corresponds to dimensionless parameters: $Re_d = 36$, $Re_f = 17\,420$, $We_d = 5285$, $We_f = 13\,125$ and $\delta/D = 0.18$. This snapshot of the ephemeral form is shown 3.18 ms after first contact of drop with pool surface. The drop contains dye causing the blue hue at the base of the crown.

ejected upon impact. Sykes *et al.* (2023) recently investigated the role of film thickness on the ejecta sheet, finding significant confinement effects if the pool is of thickness less than 0.22 times the drop diameter. Fudge *et al.* (2023) performed experiments and Basilisk simulations for the impact of immiscible liquids, focusing on the effect of the viscosity difference between the two, for moderate impact velocities. They developed a splashing threshold incorporating the viscosity ratio. Their pool was more viscous than the drop, which is the opposite configuration to the one studied herein. Tian *et al.* (2024) extended the range of impact conditions to higher Weber (We) numbers and tracked the ejection angle, bending and intricate buckling of the ejecta sheet, for miscible liquids of different viscosity ratios.

In this study, we focus on the formation of an intriguing double-crown splash, which is shown in figure 1 and forms when a high-viscosity drop impacts on a thin film of an immiscible lower viscosity oil, at impact conditions not previously studied. To pin down the underlying mechanism, we perform both experiments and high-resolution axisymmetric numerical simulations of the three-phase impact configuration. We also study the effects of changing the impact velocity, liquid properties and film thickness to find the narrow regime where this ephemeral structure appears.

2. Experiments

The double-crown phenomenon emerges following the impact of a high-viscosity glycerine drop, 1200 cP, onto a shallow pool or thin film of a lower-viscosity liquid, a 2 cSt silicone oil. The two liquids are immiscible and their properties are listed in table 1. Experiments were all carried out with the same impact velocity, but with different drop viscosity and thin-film thicknesses on the glass substrate. The drop release height was held constant at $H = 5.4$ m, resulting in an impact velocity of $U = 7.75$ m s^{-1}, measured from high-speed video clips. The highly viscous drop is slowly pinched off from a plastic nozzle with an inner diameter of 4.2 mm. The drop size is measured from the high-speed

Liquid	Density ρ (kg m^{-3})	Viscosity μ (mPa s)	Surface tension σ (mN m^{-1})	Interfacial tension σ_{df} (mN m^{-1})	D_H (mm)	D_V (mm)
Drop: Glycerine	1260	1200	64	40	5.0	3.57
Film: Silicon Oil	880	1.76	18.2	40	—	—

Table 1. Physical properties for the drop and film liquids, at room temperature of 21°C.

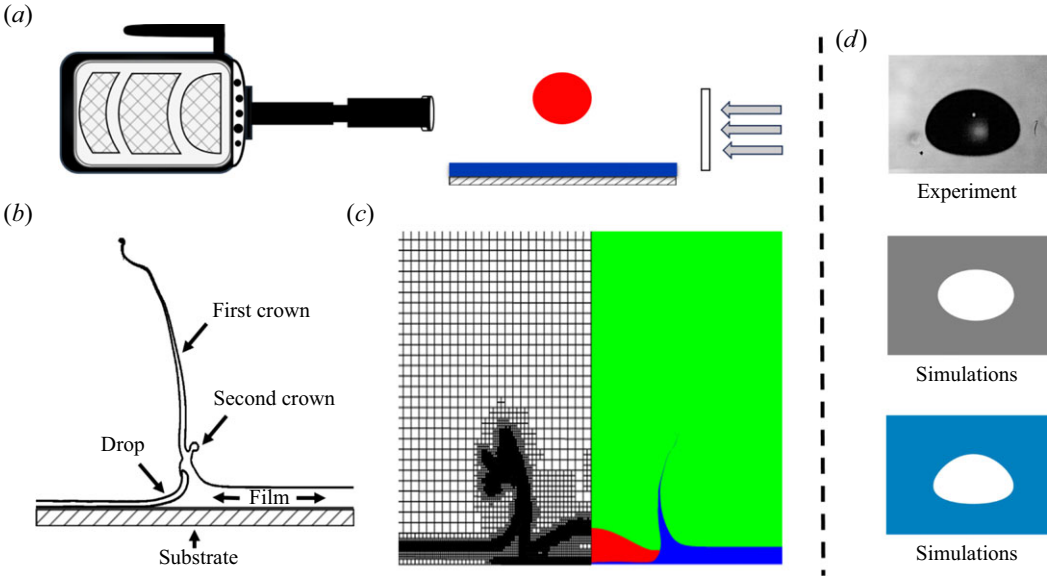

Figure 2. (*a*) A schematic of the experimental set-up. (*b*) Sketch showing the main features of the double-crown formation. (*c*) An example of axisymmetric numerical simulations, under the conditions in figure 1 at early times, showing the localised grid refinement on the left and the primary crown on the right side. The drop is coloured red, the film blue and the air green. (*d*) Drop shapes: experimental observation of the drop, with horizontal diameter $D_H = 5$ mm and vertical diameter $D_V = 3.6$ mm, just before contact (top); oblate elliptic drop (middle) and asymmetric flat-bottom drop fit used as the initial conditions for the simulations (bottom).

video frames, with D_H being the horizontal diameter, whereas D_V is its vertical diameter. The effective diameter of the drop D is estimated by $(D_H^2 D_V)^{1/3}$. The drop is noticeably flattened by air resistance during the long free-fall, as is seen in figure 2(*d*), giving an aspect ratio of $D_V/D_H \simeq 0.71$ at impact. Numerical simulations described below studied a wide range of impact conditions to mark the region where the double-crown phenomenon occurs.

The liquid is fed from a glass separator funnel equipped with a gate valve to set a slow constant flow rate to feed the drop until it pinches off by gravity. To minimise the sideways drift, away from the focal plane of the imaging, the drop is allowed to free-fall through a 5 m long plexiglass tube before hitting the liquid film. The overall crown shapes are near axisymmetric until rupture starts on the edges, as shown in video frames in supplementary figure S1.

The 2 cSt silicone oil film on the substrate is 0.80 mm thick. It sits on a microscope slide glass substrate with dimensions of 50 × 75 × 1 mm. To achieve a consistent film thickness, a fixed amount of the liquid is deposited at the centre of the glass plate using a syringe.

The liquid takes approximately 50 s to spread into a uniform film covering the entire glass plate. The time between liquid deposition and drop impact was maintained constant to minimise variability in this film thickness. Moreover, a clean glass substrate was employed for each impact to eliminate the potential for contamination from earlier drops. Our film thicknesses are consistently in the thin-film regime, as defined by Fedorchenko & Wang (2004), where the thickness is normalised by the horizontal diameter of the droplet, that is, $\delta/D_H < 0.25$.

We used a long-distance microscope with adjustable magnification (Leica APO-16) to visualise the impact dynamics. The images were captured using high-speed Phantom V2511 camera at a frame rate of 39 000 fps with a pixel resolution of 40 micron pixel^{-1}. A 350 W metal–halide Sumita lamp was used for back-side illumination of a diffuser sheet. The experimental set-up is sketched in figure 2. Additionally colour snapshots, like those in figure 1, were taken with a Nikon DSLR camera and a triggered flash. For these images, Methylene Blue powdered dye was dissolved into the glycerine to make the drops more distinguishable during impact, which slightly reduces its surface tension and viscosity by 4 % and 7 %, respectively. These slight reductions did not significantly alter the overall crown evolution.

3. Numerical simulations

To pinpoint the dynamics underlying the generation of the double crown, we apply volume-of-fluid (VOF) axisymmetric numerical simulations to reveal the velocity and vorticity fields within the liquids. We use the freely available open-source software code Basilisk, developed by Popinet and co-workers (Popinet 2015), as a versatile continuation of the Gerris code (Popinet 2003), as it can accurately handle multiple immiscible fluids and their interfaces. The power of these codes is the extreme dynamically adaptive grid refinement, allowing them to resolve the micron-thick liquid or air-sheets emerging during the splashing (Thoraval *et al.* 2012). Basilisk has also been used for computationally extreme fully three-dimensional (3-D) impact simulations (Wang *et al.* 2023), which have captured the fine splashing and entrapment of bubble-rings during the initial contact (Thoraval *et al.* 2013; Li *et al.* 2018). This code uses the VOF method to solve the incompressible Navier–Stokes equations with free surfaces. It can handle the three immiscible fluids of our impact configuration. The axisymmetric computational domain extends $6.8(D/2)$ in both radial and vertical directions, where D is the drop diameter. No-slip and impermeability boundary conditions were imposed at the bottom of the domain, while free-slip and open-flow conditions were applied both at the lateral and top boundaries. Adaptive grid-refinement conditions were employed to create small cells near the rapidly changing free interfaces and in areas with significant variations in velocity field component magnitudes. The initial conditions include the flattened shape of the drop at impact, as shown in figure 2(*d*). This was specified by an asymmetric oblate ellipsoid according to the formula $(y-h)^2 + f(y)r^2 = R^2$ with $h = 0.405$, $R = 0.25$ and $f(y) = 1.7y^2 + 0.264$.

The configuration involves three surface tensions: the drop–air surface tension is denoted by σ_d and has a value 64 mN m^{-1} for the glycerine drop, whereas the film–air surface tension $\sigma_f = 18$ mN m^{-1}. The interfacial tension σ_{df} between the glycerine droplet and the silicone oil film was set at 40 mN m^{-1}. The length and velocity scales were normalised with the effective drop diameter D and impact velocity U, respectively, whereas the time scale was non-dimensionalised using $\tau = D/U$. To ensure mesh independence in our regime of interest, a minimum cell size of 2.0 μm was required corresponding to a maximum refinement level of 12 in the domain, which is equivalent to a

uniform grid of 4096 × 4096 cells. However, the resulting adaptive grid comprised half-a-million cells (refer to figure 2), in contrast to the unfeasible 16.7 million cells for a uniform grid. The simulations required $O(10^3)$ CPU core hours and were executed in parallel across 20−40 CPUs. The simulations are capable of reproducing the experimentally observed features of the double crown, using a refinement level of 11, but were all carried out at a level of 12 using the volume fraction field with tolerance $O(10^{-3})$ and the velocity field with tolerance $O(10^{-3})$ as grid refinement criterion. The effect of refinement level on the shape of the second crown is shown in supplementary figure S2. At level 13, the computational domain contains approximately two million cells, necessitating the use of more CPUs for the parallel computing, which we find to slow down the computation excessively. For simulations at level 13, it took approximately one month to reach the stage of double-crown formation, using 40 CPUs to simulate a single case. An additional factor contributing to the extended duration was the substantial viscosity contrast between the drop and the film, which significantly decelerated the simulations.

3.1. *Parameter range*

The range of simulated impact conditions are characterised in terms of Reynolds (*Re*) and Weber numbers, based on drop or film properties:

$$Re_f = \frac{UD}{\nu_f} = 13\,000{-}34\,000; \quad Re_d = \frac{UD}{\nu_d} = 30{-}110, \tag{3.1}$$

$$We_f = \frac{\rho_f DU^2}{\sigma_f} = 7850{-}37\,000; \quad We_d = \frac{\rho_d DU^2}{\sigma_d} = 3160{-}14\,840. \tag{3.2}$$

This gives the corresponding range of Ohnesorge numbers:

$$Oh_f = \frac{\mu_f}{\sqrt{\sigma_f \rho_f D}} = 0.002{-}0.011; \quad Oh_d = \frac{\mu_d}{\sqrt{\sigma_d \rho_d D}} = 1.1{-}2.3. \tag{3.3}$$

Finally, the normalised range of film thicknesses is $\delta/D = 0.10{-}0.30$.

4. Results and discussion

4.1. *Overall double-crown formation*

Figure 3 shows the evolution of the splash and compares the experiment and numerical simulation, showing good correspondence between the two. The crown is entirely formed from the low-viscosity film liquid, while the high-viscosity drop liquid deforms into a bowl, coating the bottom of the shallow crater. The early ejecta sheet is barely visible in the second frame in the experiment, owing to the low image resolution. The initial crown emerges vertically out of the film liquid and evolves as expected (Engel 1966; Bisighini *et al.* 2010; Zhang *et al.* 2010), with its top being pulled towards the axis of symmetry and the thin sheet buckling (Marston *et al.* 2016). By definition, the buckling is absent in the axisymmetric simulation. In the fourth frame, we see the second crown emerge out of the free surface near the base of the first one. The simulation shows this occuring near the outer tip of the drop liquid, which is now stretched into a thin layer at the bottom of the crater. Keep in mind that the viscosity of the silicone oil film is much smaller than that of the glycerine drop. This allows easy deformation of the drop as it slides on the lower-viscosity fluid, reminiscent of the glycerine sliding on a thin layer of ethanol during the Marangoni breakup of a glycerine crown (Aljedaani *et al.* 2018). The second crown rises rapidly at approximately 45° to the vertical, but then forms edge instability and breaks into a myriad

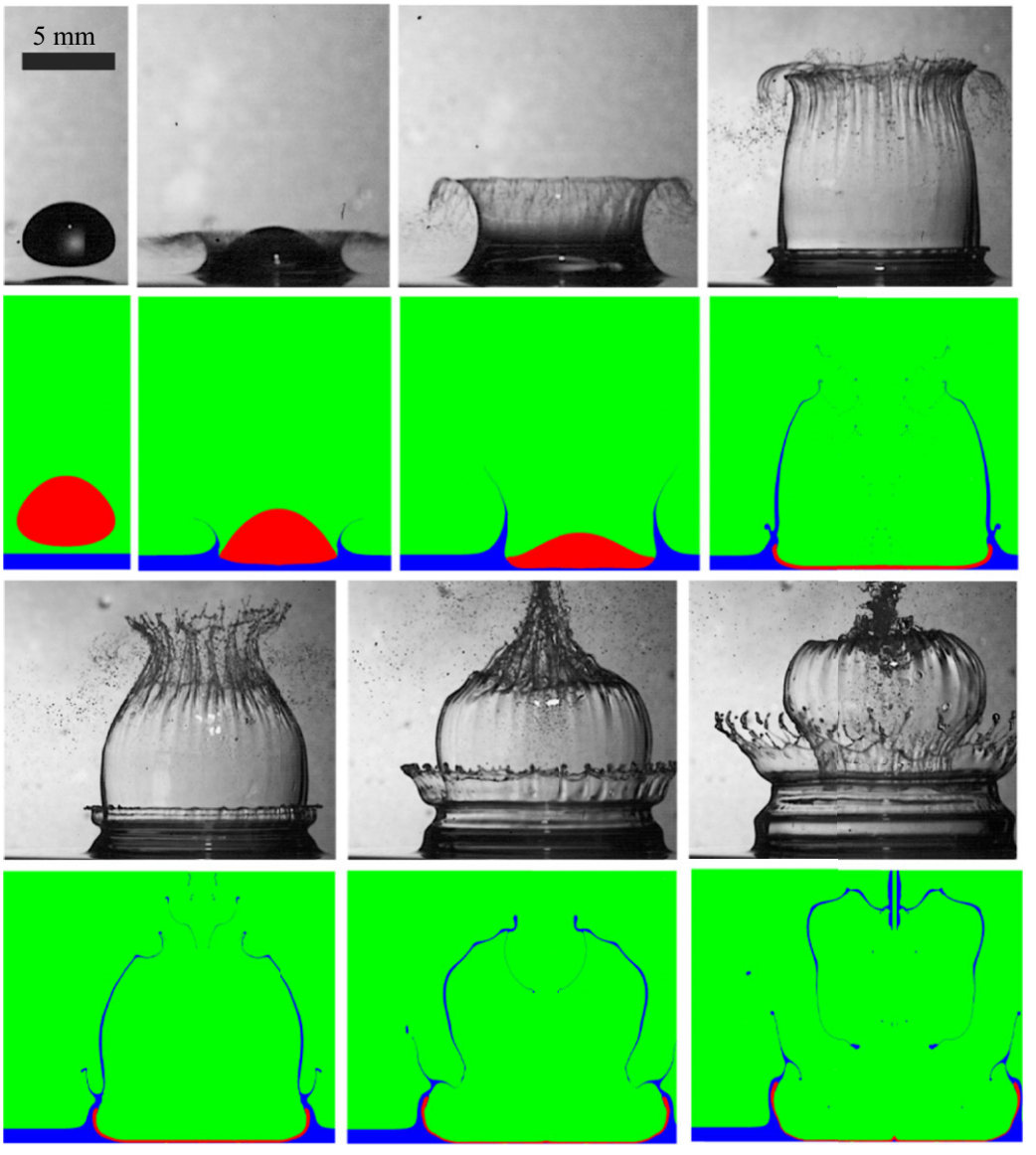

Figure 3. Comparison between experiment and axisymmetric simulation for identical impact conditions listed in figure 1. From left to right, observations at time –0.05, 0.15, 0.5, 1.73, 2.36, 3.45 and 4.84 ms. See also the movies in the supplementary material.

of tendrils which release large droplets. Such edge breakup has been extensively studied in recent years (Villermaux & Bossa 2011; Wang *et al.* 2018). The earliest horizontal ejecta sheet generates most of the fine spray, but here is an additional mechanism to produce larger droplets.

Figure 4(*a*) reveals that the second crown is driven by a pair of counter-rotating vortex rings, which travel radially and pass through the free surface, at velocity $U_v \sim 2$ m s^{-1}. Close-up viewing of the simulation, in figure 4(*b*), shows the formation of these two vortex rings, arising from the two boundary layers.

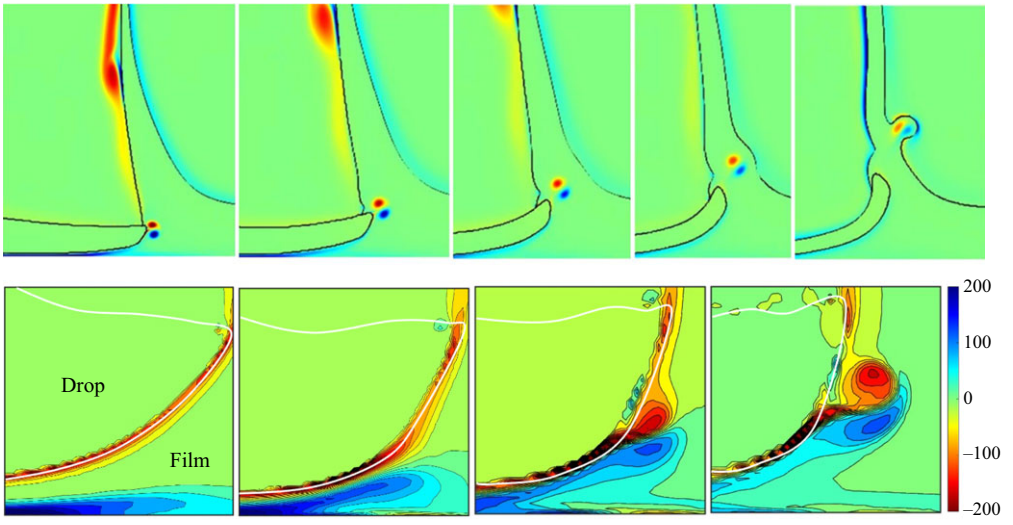

Figure 4. (*a*) Typical time sequence of a pair of vortices emerging near the tip of the extended drop, then self-propelling radially towards the outer free surface, exiting through it and forming the double crown, shown at the following times: $t/\tau = 1.24, 1.59, 2.27, 2.44, 2.78$. (*b*) Close-up contours of the vorticity field in the gap between drop and solid surface located at the bottom of the images, for $t/\tau = 0.65, 0.73, 0.82, 0.90$, showing first the separation of the vortex from the solid boundary and subsequently from the drop edge. The colour coding indicates the magnitude of the non-dimensional azimuthal vorticity.

4.2. *Vorticity production*

Since the vortex rings drive the second crown out of the free surface at the base of the regular crown, the production of their vorticity thereby plays a key role in these dynamics. In general, for drop impacts, the initial conditions have no vorticity, with a quiescent pool and a drop in uniform translation. Therefore, owing to the persistence of irrotationality theorem, the formation of vorticity during the impact deformations must occur at the interfaces, often the free surface, as is explained in detail by Thoraval, Li & Thoroddsen (2016). Robust vortex rings are generated for low Weber numbers, $We = \rho DU^2/\sigma \leqslant 64$ (Peck & Sigurdson 1994; Cresswell & Morton 1995). Thoraval *et al.* (2016) showed how a drop-impact generated vortex ring can self-destruct when it interacts with a free surface – see also Dahm, Scheil & Tryggvason (1989) and Stock, Dahm & Tryggvason (2008). This does not apply here, as $We_f \simeq 14\,500$, rather, the vorticity of these rings is produced at the solid surface and along the underside of the drop as it squeezes out the lower-viscosity silicone oil, as is seen in figure 4(*b*). The bottom of the drop flattens as it impacts the top of the film. For a pool of the same density as the drop, the interface is known to slow the drop velocity by approximately half (Hendrix *et al.* 2016; Jian *et al.* 2020). Here, the drop is much denser than the pool, 1260 versus 880 kg m^{-3}, giving a density ratio $\rho_r = \rho_{pool}/\rho_d = 0.70$, which will slow the drop down to a lesser extent. Fudge, Cimpeanu & Castrejón-Pita (2021) have studied the details of this deceleration for drops impacting deep pools. Even though their impact Re_f is much smaller, it is clear by extrapolation that in our cases, viscosity does not affect the initial interface speed, but $\overline{U} = U_i/U \simeq 1/\sqrt{1 + 2.71\rho_r + C/Re_f} = 0.588$, i.e. slightly faster than half. The presence of the solid at the bottom of the thin film will of course quickly slow down this speed, but the density difference should enhance the radial velocity in the film.

Subsequently, one can model the radial speed in the layer between the drop and the solid, as a layer of constant thickness, as shown in the inset sketch in figure 5(*a*), from the

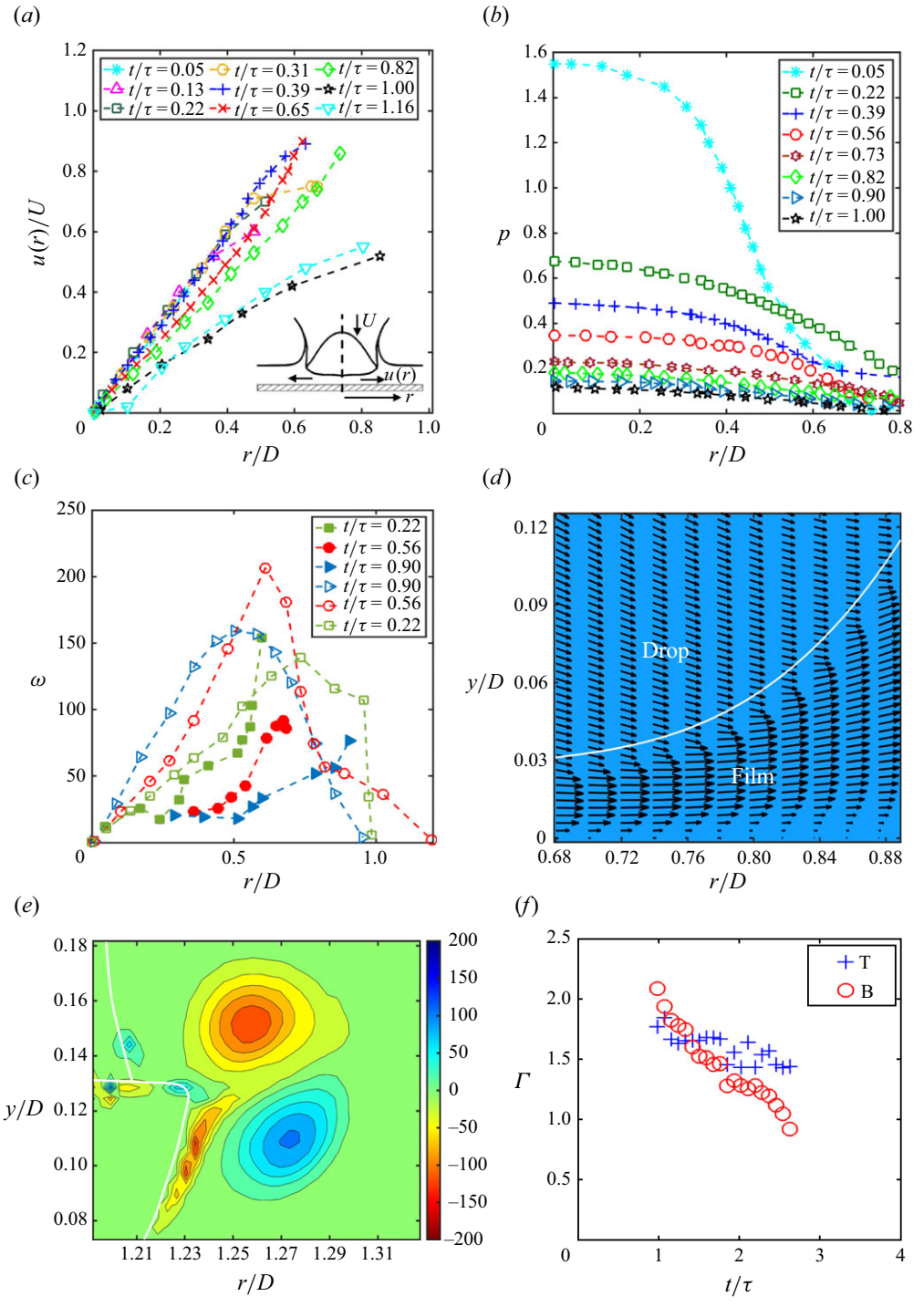

Figure 5. Characteristics of the vorticity in the vortex rings for the main case of double-crown formation, from figures 1, 3 etc. (*a*) Velocity profile of the film squeezed out from under the drop. (*b*) Pressure profile inside the film layer. (*c*) Vorticity strength in the two boundary layers, along the solid (open symbols) and drop interface (filled symbols). (*d*) Velocity profiles across film. (*e*) Iso-vorticity contours for the vortex pair at separation from the drop tip at $t/\tau = 1.26$. (*f*) Changes in the normalised circulation of the two vortices with time, until they pass through the outer free surface. 'T' indicates the top vortex and 'B' the bottom vortex.

simulation. The velocity of the drop towards the solid $V \simeq 0.6\,U$ will give a volume of liquid squeezed out of a circular region of radius $r = R$, during time $\mathrm{d}t$, as $Q = \pi R^2 V\,\mathrm{d}t$. The average radial velocity to remove this volume is $u_r(R) = Q/(2\pi R\,h) = R\,V\mathrm{d}t/(2h)$, where h is the current layer thickness. This shows a radial velocity increasing linearly with R, as is born out for early times in figure 5(*a*), until the edge of the drop moves away from the surface for $t/\tau \geqslant 1.0$. The normalised radial velocity reaches approximately 80 % of the impact velocity near the edge of the thin layer where the drop bends up. The corresponding radial pressure gradient needed to drive out this flow is shown in figure 5(*b*). The radial profiles of the magnitude of the vorticity in the two boundary layers along the solid plate and along the drop surface, are shown in figure 5(*c*), while figure 5(*d*) shows the velocity profile in the gap, transitioning from near parabolic to a uniform flow for the larger radii in the figure. The vorticity in the two boundary layers separate to form the vortex pair, with the vorticity contours shown in figure 5(*e*). Figure 5(*f*) shows the circulation of the two vortices after they separate from the drop tip until they penetrate the outer free surface to eject the second crown. The azimuthal stretching has little effect on the vorticity strength, while slow viscous diffusion reduces it slightly before they reach the outer free surface, travelling at 2.4 m s^{-1}, which is $\sim 0.3 \times U$. The vortex rings thereby easily penetrate the free surface, at a local $We_v = \rho W(0.3 \times U)^2/\sigma_f \simeq 110$ and Froude number $Fr_v = (0.3 \times U)^2/(gW) \simeq 1500$, where $W \simeq 0.4$ mm is the combined width of the two vortices in figure 5(*e*). Keep in mind that the vortices emerge at 45° to the vertical, feeling even less of the downwards gravitational pull.

The axisymmetric vorticity has only the azimuthal component, which is generated along the solid surface and the underside of the highly viscous drop; similar vorticity production was seen by a viscous drop impacting a deep pool by Li *et al.* (2017). The flux of vorticity from the solid wall can be approximated by the radial pressure gradient (Lighthill 1963), i.e.

$$\mu_f \frac{\partial \omega}{\partial y} = \frac{\partial p}{\partial r}, \tag{4.1}$$

which can be compared with the values in figures 5(*b*) and 5(*c*). A rough estimate of the circulation of the vortices can be formulated by integrating the ω-production with time up to the time of separation. The duration of the squeeze flow is $T \sim 2\delta/U \simeq 0.2$ ms, giving a boundary layer thickness of $\delta_{BL} = \sqrt{\nu_f T} \simeq 20\,\mu$m. Combining these with the characteristic $u(r) \sim 0.8 \times U$ (figure 5*a*), the vorticity strength is $\omega \sim 3 \times 10^5$ s^{-1} or 160 in the normalised coordinates in figure 5(*c*), showing good comparison. Integrating over the area of each vortex R_v gives the corresponding circulation $\Gamma \sim \omega\pi R_v^2 \sim 0.01$ m^2 s^{-1}, which is also in reasonably good agreement.

4.3. *Parameter regime with double crown*

The experiments showed that the double crown only occurs in a narrow range of parameters. Using numerical simulations to span the adjacent impact conditions, the underlying reasons become clear. The trajectory of the vortex pair is sensitive to slight changes in liquid properties and the film thickness δ, as demonstrated in figure 6, for fixed impact velocity. Here, we see that small changes in the drop and pool viscosities affect the relative strength of the two vortices, making the pair rise too fast or travel along the solid surface, in neither case do they perforate the free surface. For the lower film viscosity, in figure 6(*c*), the inset shows that the bottom vortex generated at the sold surface is stronger that the top one generated at the viscosity-jump at the bottom of the drop, directing the vortex pair towards the solid surface, keeping them away from the free surface and thereby

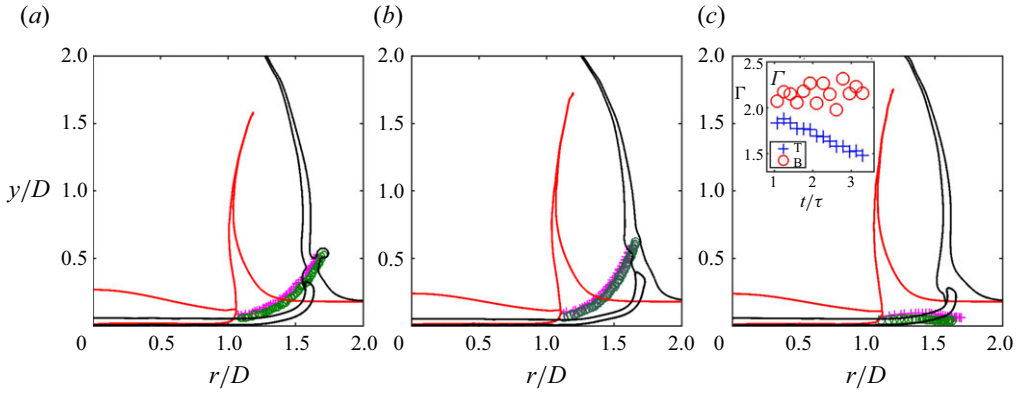

Figure 6. Trajectories of the vortex pair for different viscosities, for a fixed film thickness of $\delta/D = 0.18$, shown from the time they separate from the edge of the drop (red curves) until they reach the outer free surface (black curves). The corresponding outlines of the drop and crown are shown at the times $t/\tau = 1.07$ (red curves) and $t/\tau = 2.95$ (black curves). The latter time is selected to show the emergence of the second crown, when the vortices rise out of the outer free surface in panel (*a*). (*a*) Impact conditions that generate the double crown, for $Oh_d = 1.83$, $Oh_f = 0.0065$ and $Re_f = 17\,420$. (*b*) A case with lower drop viscosity where no secondary crown is formed, for $Oh_d = 1.16$, $Oh_f = 0.0065$ and $Re_f = 17\,420$. (*c*) A case with lower film viscosity where no secondary crown is formed and the vortices translate along the solid substrate, for $Oh_d = 1.83$, $Oh_f = 0.004$ and $Re_f = 27\,714$. The inset shows that the bottom vortex is stronger than the top one, bringing the top vortex towards the solid surface. The centres of the upper and lower vortices are marked by + and o symbols respectively.

preventing the double crown. Figure 7(*a*,*b*) maps the boundaries of the regime where the double crown occurs, for the range of the two viscosities and the film thickness.

Finally, we have varied the drop impact velocity in the simulations, over a range of film thicknesses, with the results shown in figure 7(*c*). Along the vertical dashed line, passing through the base case in figure 1, one sees that the double crown forms for impact velocities from 7 to 12 m s^{-1}. At the extremes in this velocity range, the vortices self-destruct by interacting with the adjacent interfaces. For the largest velocities, this interaction is with the drop surface, while for the lowest velocity, the vortices interact with the free surface between the film and air. At the large-velocity side, this interaction is determined by the speed of the vortex pair and whether they can outrun the tip of the rapidly spreading flattened drop. This translational speed U_v, in figure 7(*d*), shows that when normalised by the impact velocity, it is nearly constant at $U_v/U \simeq 0.23$ until $U \simeq 10$ m s^{-1}, above which, this ratio reduces abruptly, suggesting a qualitative change. The circulation of the vortices for $U = 10$ m s^{-1} is shown in figure 8(*a*). Here, Γ has a larger value than for $U = 7.75$ m s^{-1} (figure 5*f*), but reduces more rapidly with time. For even larger impact velocities $U = 11$ and 13 ms^{-1}, the circulation is weaker and reduces quickly to near-zero (figure 8*b*,*c*). Close-up study of the vortices, in figure 9, shows that, for the large $U = 13$ m s^{-1}, the vortices cannot outrun the edge of the viscous drop. Instead, they self-destruct in the following way. The isolated vortices sit next to the much more viscous drop, which acts effectively like a solid surface. The circulating flow past it generates a boundary layer with opposite sign vorticity next to the interface, which interacts with them and reduces their intensity and induces opposite direction velocity. Figure 9(*a*,*b*) shows how the boundary layers are pulled in between the two vortices, thereby reducing their strength, advection speed and eventually separating them on the two sides of the tip of the drop liquid in figure 9(*c*,*d*).

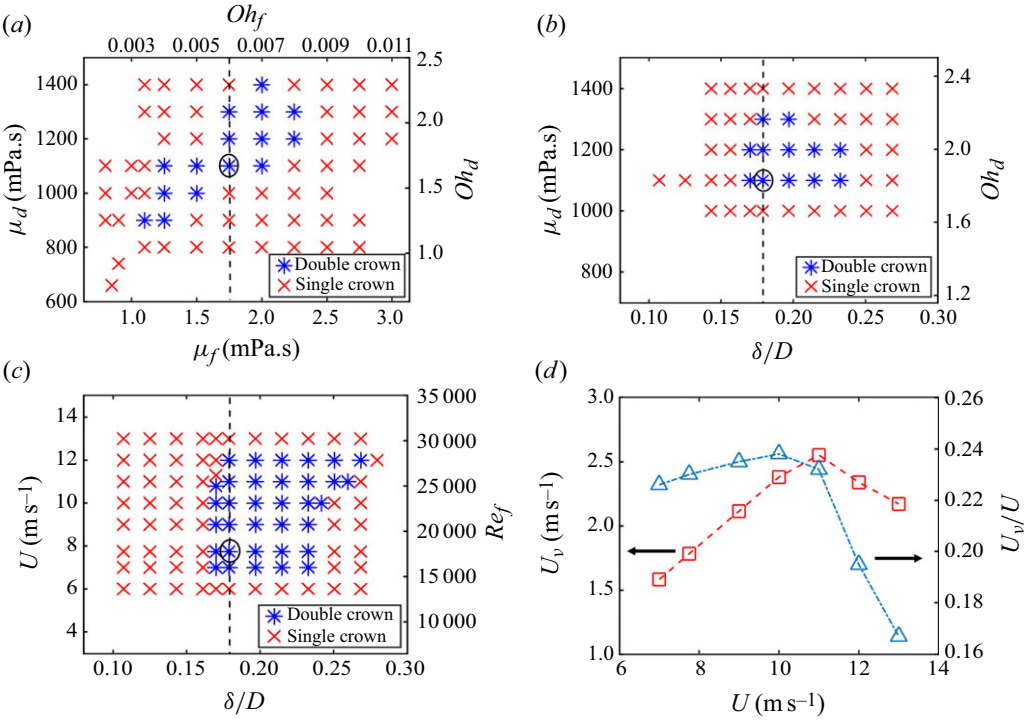

Figure 7. A parametric map for the single- and double-crown formation, based on the numerical simulations. (*a*) Film thickness is fixed at $\delta/D = 0.18$, while we vary the drop and film viscosities. (*b*) Film viscosity fixed at $\mu_f = 1.75$ mPa s^{-1} ($Oh_f = 0.0065$), while varying drop viscosity and film thickness. The corresponding drop Ohnesorge numbers Oh_d in panels (*a*) and (*b*), based on drop viscosity, are shown on the right-side ordinate. (*c*) Effect of impact velocity. The film viscosity is fixed at $\mu_f = 1.75$ mPa s^{-1} ($Oh_f = 0.0065$), while the impact velocity and film thickness are varied. The right-side ordinate shows the film Reynolds number Re_f. The vertical dashed lines in panels (*a*) and (*b*) mark the parameter planes in the opposite panel. The symbols identify all conditions simulated, with the stars marking where the double crown is formed. The black circles identify the double-crown experimental case, shown in figures 1, 3–5. (*d*) Vortex speed versus impact velocity, along the vertical dashed line in panel (*c*). The right ordinate shows the vortex velocity normalised by the impact velocity.

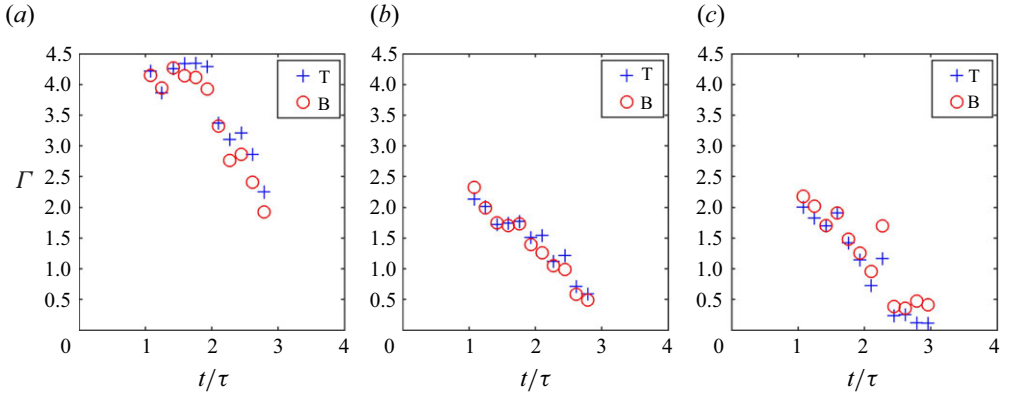

Figure 8. Rapid reduction in the circulation of the two vortices with time for the largest impact velocities: (a) $U = 10$ m s^{-1}, (b) $U = 11$ m s^{-1} and (c) $U = 13$ m s^{-1}. Conditions are the same as along the vertical line in figure 7(*c*).

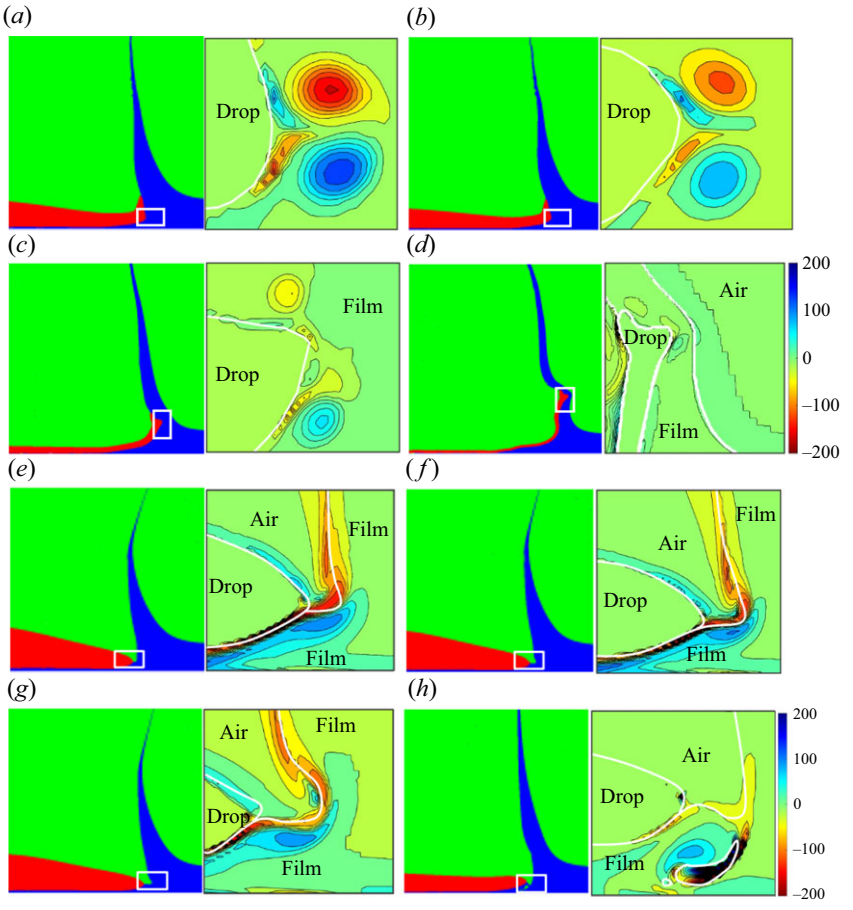

Figure 9. (*a–d*) Self-destruction of the vortices, by interacting with the drop surface, for the largest impact velocity $U = 13$ m s^{-1}, shown at the following times: $t/\tau = 1.25, 1.88, 2.56, 3.67$, for $\delta/D = 0.18$, $Oh_d = 1.83$, $Oh_f = 0.0065$ and $Re_f = 29\,220$. The left side of each panel shows the fluids, drop (red), film (blue) and air (green), while the right side shows the strength of the azimuthal vorticity, with the normalised values identified by the colour bar. The white lines mark the interfaces between two of the three fluids. (*e–h*) Self-destruction of the vortices for the lower impact velocity at $U = 6$ m s^{-1}, when the bottom vortex pulls in an air cavity, shown at the following times: $t/\tau = 1.0, 1.07, 1.11, 1.70$, for $\delta/D = 0.18$, $Oh_d = 1.83$, $Oh_f = 0.0065$ and $Re_f = 13486$.

For the boundary at the lower impact velocity, a different mechanism blocks the progression of the vortices, preventing the double crown. The lower panels of figure 9 show an example of this. Here, at lower Re_d, the viscosity of the drop reduces its deformation, as seen by the thicker edge of the drop. This allows the film to move ahead of the drop and the free surface approaches its tip. The vortices then deform the free surface and self-destruct, by pulling in a bubble in panel (*h*). This is reminiscent of the primary vortex ring generated by a crop impacting on a deep pool, studied by Thoraval *et al.* (2016). They showed that the strongest vortices, generated by oblate drops, self-destructed by interacting with the free surface.

Furthermore, our simulations show that rather subtle changes in the bottom shape of the drop play a determining role in the formation of the double crown. Ellipsoidal drop travels longer vertically before it is projected in the horizontal direction, under the free surface of the film, thereby pushing the film sideways and making the free surface and air

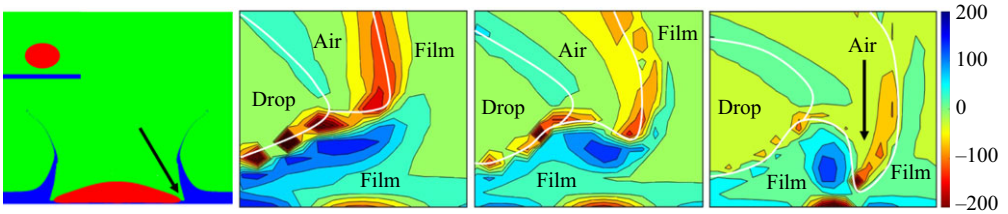

Figure 10. Impact of an ellipsoidal drop, where the double crown does not form. The vorticity field shown at normalised times: $t/\tau = 1.02$, 1.11, 1.12, for $\delta/D = 0.18$, $Oh_d = 1.83$, $Oh_f = 0.0065$ and $Re_f = 17\,420$.

penetrate along the drop towards the solid surface, thereby blocking the progression of the top vortex, as shown in figure 10.

5. Conclusions

The plethora of possible ejecta and crown formations which can occur during drop impacts on liquid surfaces are multiplied when one allows the drop and pool or film to have different liquid properties. While useful results can certainly be extracted from systematic studies across the vastness of this parameter space, identifying qualitative changes or bifurcation in the crown or ejecta shapes can sometimes be pinpointed by fortuitous discoveries of novel flow phenomena. Herein, we have studied a new parameter regime, where we have found such a new mechanism, where the formation of two vortex rings drives a second splashing crown out of the free surface. We explain the formation of these vortices and map the narrow range of parameters where they rule this ephemeral phenomenon. In essence, the trajectory of the vortex pair is sensitive to the difference in their strength, which is governed by the vorticity production at the boundaries of the expelled flow in the gap as the drop approaches the solid wall, which in turn is determined by the film thickness and drop viscosity. The bottom shape of the drop is also shown to be important for this phenomenon. This reinforces that for drops larger than the capillary length, one must include this effect. This intricate interplay between many factors limits the phenomenon to a narrow range of impact conditions, while highlighting a generic mechanism, which could influence splashing in other ways. For example, the last panel in figure 3 shows clearly that the double crown greatly enhances the splashing of large droplets, now from the breakup of the second edge, into prominent extended tendrils. We expect similar results to apply even if the drop and pool are miscible, as long as the large viscosity difference is maintained.

Supplementary material and movies: Supplementary material and movies are available at https://doi.org/10.1017/jfm.2025.108

Funding. This study was supported by King Abdullah University of Science and Technology (KAUST) under Grants Nos. URF/1/2621-01-01 & BAS/1/1352-01-01.

Declaration of interests. The authors report no conflict of interest.

References

Agbaglah, G.G. 2021 Breakup of thin liquid sheets through hole–hole and hole–rim merging. *J. Fluid Mech.* **911**, A23.

Aljedaani, A.B., Wang, C., Jetly, A. & Thoroddsen, S.T. 2018 Experiments on the breakup of drop-impact crowns by Marangoni holes. *J. Fluid Mech.* **844**, 162–186.

Bisighini, A., Cossali, G.E., Tropea, C. & Roisman, I.V. 2010 Crater evolution after the impact of a drop onto a semiinfinite liquid target. *Phys. Rev. E* **82**, 036319.

BLANCHARD, D.C. & WOODCOCK, A.H. 1957 Bubble formation and modification in the sea and its meteorological significance. *Tellus* **9** (2), 145–158.
CHEN, N., CHEN, H. & AMIRFAZLI, A. 2017 Drop impact onto a thin film: miscibility effect. *Phys. Fluids* **29** (9), 092106.
CRESSWELL, R.W. & MORTON, B.R. 1995 Drop-formed vortex rings – the generation of vorticity. *Phys. Fluids* **7** (6), 1363–1370.
DAHM, W.J.A., SCHEIL, C.M. & TRYGGVASON, G. 1989 Dynamics of vortex interaction with a density interface. *J. Fluid Mech.* **205**, 1–43.
DEEGAN, R.D., BRUNET, P. & EGGERS, J. 2007 Complexities of splashing. *Nonlinearity* **21** (1), C1.
EDGERTON, H.E. & KILLIAN, J.R. 1939 *Flash: Seeing the Unseen by Ultra High-Speed Photography*. Charles T. Branford Co.
ENGEL, O.G. 1966 Crater depth in fluid impacts. *J. Appl. Phys.* **37** (4), 1798–1808.
FEDORCHENKO, A.I. & WANG, A.-B. 2004 On some common features of drop impact on liquid surfaces. *Phys. Fluids* **16** (5), 1349–1365.
FUDGE, B.D., CIMPEANU, R., ANTKOWIAK, A., CASTREJÓN-PITA, J.R. & CASTREJÓN-PITA, A.A. 2023 Drop splashing after impact onto immiscible pools of different viscosities. *J. Colloid Interface Sci* **641**, 585–594.
FUDGE, B.D., CIMPEANU, R. & CASTREJÓN-PITA, A.A. 2021 Dipping into a new pool: the interface dynamics of drops impacting onto a different liquid. *Phys. Rev. E* **104**, 065102.
FUDGE, B.D., CIMPEANU, R. & CASTREJÓN-PITA, A.A. 2024 Drop impact onto immiscible liquid films floating on pools. *Sci. Reports* **14**, 13671.
GEPPERT, A., CHATZIANAGNOSTOU, D., MEISTER, C., GOMAA, H., LAMANNA, G. & WEIGAND, B. 2016 Classification of impact morphology and splashing/deposition limit for n-hexadecane. *Atomiz. Sprays* **26** (10), 983–1007.
GEPPERT, A., TERZIS, A., LAMANNA, G., MARENGO, M. & WEIGAND, B. 2017 A benchmark study for the crown-type splashing dynamics of one-and two-component droplet wall–film interactions. *Exp. Fluids* **58**, 1–27.
HENDRIX, M.H.W., BOUWHUIS, W., VAN DER MEER, D., LOHSE, D. & SNOEIJER, J.H. 2016 Universal mechanism for air entrainment during liquid impact. *J. Fluid Mech.* **789**, 708–725.
JIAN, Z., CHANNA, M.A., KHERBECHE, A., CHIZARI, H., THORODDSEN, S.T. & THORAVAL, M.-J. 2020 To split or not to split: dynamics of an air disk formed under a drop impacting on a pool. *Phys. Rev. Lett.* **124** (18), 184501.
KIM, D., LEE, J., BOSE, A., KIM, I. & LEE, J. 2021 The impact of an oil droplet on an oil layer on water. *J. Fluid Mech.* **906**, A5.
KITTEL, H.M., ROISMAN, I.V. & TROPEA, C. 2018 Splash of a drop impacting onto a solid substrate wetted by a thin film of another liquid. *Phys. Rev. Fluids* **3** (7), 073601.
LI, E.Q., BAILHARZ, D. & THORODDSEN, S.T. 2017 Vortex-induced buckling of a viscous drop impacting a pool. *Phys. Rev. Fluids* **2** (7), 073602.
LI, E.Q., THORAVAL, M.-J., MARSTON, J.O. & THORODDSEN, S.T. 2018 Early azimuthal instability during drop impacts. *J. Fluid Mech.* **848**, 821–835.
LIANG, G. & MUDAWAR, I. 2016 Review of mass and momentum interactions during drop impact on a liquid film. *Int. J. Heat Mass Trans* **101**, 577–599.
LIGHTHILL, M.J. 1963 *Part II of Laminar Boundary Layers (Ed. L. Rosenhead)*. Oxford University Press.
LOHSE, D. 2022 Fundamental fluid dynamics challenges in inkjet printing. *Annu. Rev. Fluid Mech.* **54** (1), 349–382.
MARCOTTE, F., MICHON, G.-J., SÉON, T. & JOSSERAND, C. 2019 Ejecta, corolla, and splashes from drop impacts on viscous fluids. *Phys. Rev. Lett.* **122** (1), 014501.
MARSTON, J.O., TRUSCOTT, T.T., SPEIRS, N.B., MANSOOR, M.M. & THORODDSEN, S.T. 2016 Crown sealing and buckling instability during water entry of spheres. *J. Fluid Mech.* **794**, 506–529.
MINAMI, F. & HASEGAWA, K. 2022 Cavity and jet formation after immiscible droplet impact into deep water pool. *Phys. Fluids* **34** (3), 033315.
MURPHY, D.W., LI, C., D'ALBIGNAC, V., MORRA, D. & KATZ, J. 2015 Splash behaviour and oily marine aerosol production by raindrops impacting oil slicks. *J. Fluid Mech.* **780**, 536–577.
PECK, B. & SIGURDSON, L. 1994 The three-dimensional vortex structure of an impacting water drop. *Phys. Fluids* **6** (2), 564–576.
POPINET, S. 2003 Gerris: a tree-based adaptive solver for the incompressible Euler equations in complex geometries. *J. Comput. Phys.* **190** (2), 572–600.
POPINET, S. 2015 A quadtree-adaptive multigrid solver for the Serre–Green–Naghdi equations. *J. Comput. Phys.* **302**, 336–358.

REIN, M. 1993 Phenomena of liquid drop impact on solid and liquid surfaces. *Fluid Dyn. Res.* **12** (2), 61–93.
ROISMAN, I.V., HORVAT, K. & TROPEA, C. 2006 Spray impact: Rim transverse instability initiating fingering and splash, and description of a secondary spray. *Phys. Fluids* **18** (10), 102104.
STOCK, M.J., DAHM, W.J.A. & TRYGGVASON, G. 2008 Impact of a vortex ring on a density interface using a regularized inviscid vortex sheet method. *J. Comput. Phys.* **227** (21), 9021–9043.
SYKES, T.C., CIMPEANU, R., FUDGE, B.D., CASTREJÓN-PITA, J.R. & CASTREJÓN-PITA, A.A. 2023 Droplet impact dynamics on shallow pools. *J. Fluid Mech.* **970**, A34.
THORAVAL, M.-J., LI, Y. & THORODDSEN, S.T. 2016 Vortex ring induced large bubble entrainment in drop impact. *Phys. Rev. E* **93** (3), 033128.
THORAVAL, M.-J., TAKEHARA, K., ETOH, T.G., POPINET, S., RAY, P., JOSSERAND, C., ZALESKI, S. & THORODDSEN, S.T. 2012 Von Kármán vortex street within an impacting drop. *Phys Rev. Lett* **108** (26), 264506.
THORAVAL, M.-J., TAKEHARA, K., ETOH, T.G. & THORODDSEN, S.T. 2013 Drop impact entrapment of bubble rings. *J. Fluid Mech.* **724**, 234–258.
THORODDSEN, S.T. 2002 The ejecta sheet generated by the impact of a drop. *J. Fluid Mech.* **451**, 373–381.
THORODDSEN, S.T., ETOH, T.G. & TAKEHARA, K. 2006 Crown breakup by Marangoni instability. *J. Fluid Mech.* **557**, 63–72.
THORODDSEN, S.T., ETOH, T.G. & TAKEHARA, K. 2008 High-speed imaging of drops and bubbles. *Annu. Rev. Fluid Mech.* **40** (1), 257–285.
TIAN, Y.S., ALJEDAANI, A.B., ALGHAMDI, T. & THORODDSEN, S.T. 2024 Dancing ejecta. *J. Fluid Mech* **981**, A4.
VILLERMAUX, E. 2020 Fragmentation versus cohesion. *J. Fluid. Mech* **898**, P1.
VILLERMAUX, E. & BOSSA, B. 2011 Drop fragmentation on impact. *J. Fluid. Mech* **668**, 412–435.
WALKER, T.W., LOGIA, A.N. & FULLER, G.G. 2015 Multiphase flow of miscible liquids: jets and drops. *Exp. Fluids* **56** (5), 106.
WANG, H., LIU, S., BAYEUL-LAINE, A.-C., MURPHY, D.W., KATZ, J. & COUTIER-DELGOSHA, O. 2023 Analysis of high-speed drop impact onto deep liquid pool. *J. Fluid Mech.* **972**, A31.
WANG, Y., DANDEKAR, R., BUSTOS, N., POULAIN, S. & BOUROUIBA, L. 2018 Universal rim thickness in unsteady sheet fragmentation. *Phys. Rev. Lett.* **120** (20), 204503.
WEISS, D.A. & YARIN, A.L. 1999 Single drop impact onto liquid films: neck distortion, jetting, tiny bubble entrainment, and crown formation. *J. Fluid Mech.* **385**, 229–254.
YARIN, A.L. 2006 Drop impact dynamics: splashing, spreading, receding, bouncing. *Annu. Rev. Fluid Mech.* **38** (1), 159–192.
YARIN, A.L. & WEISS, D.A. 1995 Impact of drops on solid surfaces: self-similar capillary waves, and splashing as a new type of kinematic discontinuity. *J. Fluid Mech.* **283**, 141–173.
ZHANG, L.V., BRUNET, P., EGGERS, J. & DEEGAN, R.D. 2010 Wavelength selection in the crown splash. *Phys. Fluids* **22** (12), 122105.
ZHANG, X., WANG, C. & RUI, S. 2022 Phenomena of single water droplet impacting a heptane layer on water pool. *Eur. J. Mech. B Fluids* **92**, 65–74.